Experimental characterization and numerical modelling of fracture processes in granite

Francesco Parisio [a,*], Ali Tarokh [b], Roman Makhnenko [b], Dmitri Naumov [a], Xing-Yuan Miao [a,c], Olaf Kolditz [a,c], Thomas Nagel [a,d,1]

[a] *Department of Environmental Informatics, Helmholtz Centre for Environmental Research – UFZ, Leipzig, Germany*
[b] *Department of Civil and Environmental Engineering, University of Illinois at Urbana-Champaign, USA*
[c] *Applied Environmental Systems Analysis, Technische Universität Dresden, Dresden, Germany*
[d] *Department of Mechanical and Manufacturing Engineering, School of Engineering, Trinity College Dublin, College Green, Dublin, Ireland*

A R T I C L E   I N F O

A B S T R A C T

Failure in brittle rock happens because micro-cracks in the crystal structure coalesce and form a localized fracture. The propagation of the fracture is in turn strongly influenced by dissipation in the fracture process zone. The classical theory of linear elastic fracture mechanics falls short in describing failure when the dissipation in the fracture process zone is non-negligible; thus, a non-linear theory should be employed instead. Here we present a study in which we explore the characteristics of the fracture process zone in granite. We have combined fracture tests on Adelaide black granite with acoustic emission detection and finite element analyses by using a non-local integral plastic-damage constitutive theory. We have further employed the theory of configurational mechanics to support our interpretation of the evolution of the fracture process zone with strong energy-based arguments. We demonstrate that the size of the fracture process zone is non-negligible and dissipative phenomena related to micro-cracking play an important role. Our results indicate this role should be assessed case by case, especially in laboratory-sized analyses, which mostly deflect from theories of both size-independent plasticity and linear elastic fracture mechanics. When strong non-linearities occur, we show that fracture energy can be correctly computed with the help of configurational mechanics and that complex numerical simulation techniques can substantially facilitate the interpretation of experiments designed to highlight the dominant physical mechanisms driving fracture.

1. Introduction

Understanding the mechanism of fracture in rock is crucial because it often acts as a precursor to the ultimate failure. Study of the fracture process zone, a localized finite zone of micro-cracks ahead of the crack tip, is essential to gain information on the physics of crack initiation (Lockner et al., 1991). Size effects, known to characterize the fracture behaviour of rock (Le et al., 2011), pose obvious difficulties in scaling the fracture behaviour from relatively small sizes suitable for laboratory experiments to the conditions encountered in large-scale application. The goal of this contribution is to shed light on the fracture mechanics aspects, particularly on size effects and crack-tip process zone in granite, by employing an integrated experimental and numerical approach that combines advanced techniques of acoustic emission detection, non-local continuous damage mechanics and configurational mechanics.

Granite, an igneous rock composed, for the most part, of silica and alumina, forms the bulk of the earth's upper crust. Because of its relative abundance, it has been the object of thorough investigations in the geoscience and geoengineering communities (Lockner et al., 1991; Watanabe et al., 2017b). At conditions far from the brittle–ductile transition temperature and pressure (Horii and Nemat-Nasser, 1986; Rutter and Neumann, 1995; Violay et al., 2017), much of the physical behaviour of granite is determined by its propensity toward fracture initiation and propagation. This has important consequences for structural failure, as in brittle mate-

rials in general (Berto and Lazzarin, 2014), and for enhancing the mass and energy transport properties because fracture permeability is several orders of magnitude higher than matrix permeability (Watanabe et al., 2017a). Granite-like materials play an important role as barriers for nuclear waste (McCarthy et al., 1978) and CO_2 storage (Metz et al., 2005), and as reservoirs for enhanced geothermal systems (Barbier, 2002). When serving a barrier function, conditions leading to fracturing need to be avoided or minimized (Council, 2013). In geothermal energy extraction, on the contrary, fracturing becomes the central subject of investigations, with the aim of drastically increasing reservoir permeability without inducing significant seismicity (Evans et al., 2005; Häring et al., 2008).

Size dependency in the fracturing behaviour of rocks has been thoroughly studied (Schmidt, 1976; Schmidt and Lutz, 1979; Chong et al., 1989; Bažant and Kazemi, 1990; Labuz and Biolzi, 1998). In general, the classical theory of linear elastic fracture mechanics (LEFM) can be successfully applied if the dissipation ahead of the crack tip is negligible with respect to the total dissipated energy (Ouchterlony, 1990; Matsuki et al., 1991; Kuruppu et al., 2014; Wegst et al., 2015). Researchers have agreed that dissipation in the fracture process zone (FPZ) manifests itself in apparent size effects of the structural behaviour (Bažant and Planas, 1997; Labuz et al., 1985; Wang et al., 1990; Zang et al., 2000; Biolzi et al., 2011). Grain size (Barton, 1982; Brooks et al., 2012; Tarokh and Fakhimi, 2014) and specimen size (Zietlow and Labuz, 1998; Otsuka and Date, 2000; Tarokh et al., 2012; Fakhimi and Tarokh, 2013; Tarokh et al., 2017) are the dominant factors influencing the role of dissipation in the fracture process zone. In granite, as in other brittle materials, the inelastic dissipation processes in the fracture process zone are mostly related to micro-crack growth and plastic flow in the material crystals: coalescence of the micro-cracks upon increased loading leads to macroscopic fractures and material splitting (Horii and Nemat-Nasser, 1986).

Several experimental techniques have been successfully applied in this context, among which are photoelastic coatings (Jankowski and Styś, 1990), three-dimensional acoustic emissions analysis (Mihashi et al., 1991), laser speckle interferometry (Wang et al., 1990), digital image correlation (Wu et al., 2011), environmental scanning electron microscopy (Brooks et al., 2013), X-ray micro-computed tomography (Skarżyński and Tejchman, 2016) and X-ray radiography (Vavro et al., 2017). While most of the laboratory characterization efforts have been dedicated to concrete (Jankowski and Styś, 1990; Mihashi et al., 1991; Wu et al., 2011; Skarżyński and Tejchman, 2016) as a readily available and standardized manufactured material, only a few examples exist for granite (Wang et al., 1990), marble (Wang et al., 1990; Brooks et al., 2013) and sandstone (Vavro et al., 2017). The experiments have highlighted several common trends in the fracture process zone:

- The width of the process zone seems to be influenced by the size of the aggregate or grain (Mihashi et al., 1991; Wang et al., 1990), conveniently referred to as the particle size, and the structural dimensions, such as the initial length of the notch (Wang et al., 1990). A smaller particle size relative to the depth of the notch implies a reduction of noise (related here to non-homogeneity of the granular material), a smaller fracture process zone width and a shift toward linear elastic fracture mechanics (Tarokh and Fakhimi, 2013).

- In general, the extension of the process zone ahead of the crack tip is independent of the heterogeneities (Mihashi et al., 1991), but it is strongly influenced by the depth of the notch relative to the height of the beam (Wu et al., 2011). The increase in notch depth causes a decrease in the length of the fracture process zone, shifting the problem characteristics toward linear elastic fracture mechanics (smaller dissipation).

In other words, the size effects are primarily influenced by the size of various heterogeneities in relation to the structural dimensions. Given the strong non-linearities involved, it is difficult to make a priori statements regarding the development of the fracture process zone and the interdependencies of the different factors involved. It is also insufficient and misleading to look at the structural response exclusively from a global perspective. Only detailed analyses of the physical mechanisms responsible for the growth and evolution of the fracture process zone can provide a comprehensive picture. Non-linear numerical simulations can contribute to the clarification effort when consistently integrated with experimental programmes. Non-linear fracture mechanical problems can be investigated within the framework of the local approach to fracture (Lemaitre et al., 2009; Murakami, 2012) and continuum damage mechanics, coupled with or uncoupled from plasticity. These methods have proved numerous times to be theoretically sound and numerically robust tools for delivering reliable modelling results and interpreting the failure of brittle materials (Parisio et al., 2015; Havlásek et al., 2016; Cervera et al., 2017; Nguyen et al., 2017; Parisio et al., 2018). To avoid the spurious mesh-size effects typical of damage mechanics and other softening constitutive models and to restore the well-posedness of the rate problem, several regularization techniques can be applied, such as viscoplastic regularizations (Needleman, 1988; Loret and Prevost, 1990; Niazi et al., 2013), non-local integral formulations (Bažant and Jirásek, 2002), gradient of internal variable formulations (Comi, 1999; Lyakhovsky et al., 2011), and models with enhanced kinematics (Dietsche et al., 1993; Chambon et al., 2001; Collin et al., 2006; Fernandes et al., 2008; Lakes, 2018). Non-local formulations based on integral averaging are effective in restoring well-posedness, although an efficient numerical implementation is complex (Jirásek, 2004; Jirásek and Marfia, 2005; Duddu and Waisman, 2013). All the above-mentioned methods have in common the introduction of a characteristic length[2], which can be related to the distribution of heterogeneities in the micro-structure. By coupling the integral non-local plastic-damage model with the theory of configurational mechanics, additional information on the local evolution of the fracture process zone can be provided in the spirit of moving phase boundaries and thermodynamic driving forces (Gross et al., 2003; Liebe et al., 2003; Timmel et al., 2009; Nagel and Kelly, 2012; Özenç et al., 2014; Parisio et al., 2018).

Numerical simulations can yield valuable physical insights, guide the interpretation of experimental results and serve as a predictive tool, provided they can faithfully represent and describe the dominant physical mechanisms. The goals of this study are precisely: (i) To undertake a comprehensive and holistic experimental and numerical analysis of the fracture behaviour of granite; (ii) to correlate the local non-linear behaviour with the global response in a systematic way and (iii) to incorporate micro-structural information and dissipation-driving forces by accounting for non-locality and configurational descriptors. We aimed to characterize, both experimentally and numerically, the kinetics of the fracture process zone and its effects on the size dependency of the structural behaviour.

The manuscript is organized as follows. In Section 2, we present the material under investigation, which is Adelaide black granite, along with the experimental procedure, composed of three-point bending tests on notched samples of different sizes. During testing, acoustic emission are continuously monitored to evaluate the evolution of the fracture process zone. In Section 3, we introduce the non-local plastic-damage constitutive model employed for numerical analyses, and we discuss its implementation in the open-

---

[2] For viscoplastic regularization, a characteristic length is substituted by a characteristic time which, in conjunction with the process time, effectively implies a length scale.

a

b

c
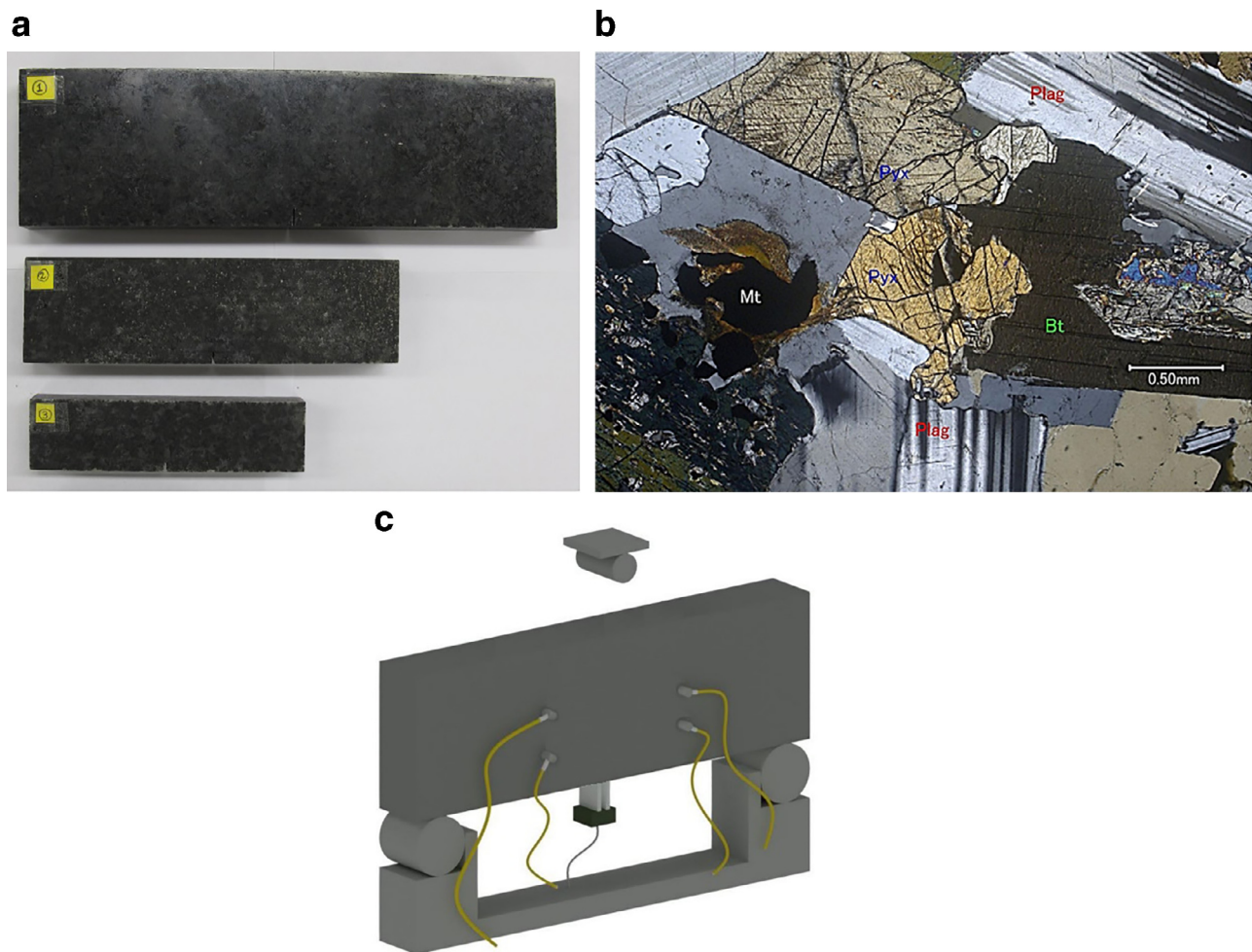
Fig. 1. (a) Scaled rock beams of Adelaide black granite and (b) view of a thin section under cross-polarized transmitted light. The minerals indicated in the picture are plagioclase (Plag), pyroxene (Pyx), biotite (Bt), and magnetite (Mt). (c) Schematic view of the apparatus employed for the three-point bending tests with the loading configuration, position of the acoustic emission sensors and the measuring device for the crack mouth opening displacement (CMOD).

source code OpenGeoSys (Kolditz et al., 2012). The calibration of material parameters is based on an independent set of experiments and micro-structural observations so that the analyses can be considered semi-blind predictions. In Section 4, we briefly outline the theory of configurational mechanics to investigate the kinematics of phase boundaries and to improve the interpretation of the fracture process zone evolution. The results of the experimental and numerical analyses along with the discussion of the most important findings are presented in Section 5. Finally, in Section 6, we draw some specific and general conclusions.

2. Experimental procedure

2.1. Rock properties

A series of three-point bending tests with a centered notch were performed on Adelaide black granite (see Fig. 1(a)). This rock consists of plagioclase ($45 - 50$ %) and pyroxene ($20 - 25$ %) with minor biotite (10 %), amphibole (5 %), magnetite (5 %) and quartz ($1 - 2$ %), which are clearly identified in thin sections under cross-polarized transmitted light, as shown in Fig. 1(b). On the basis of these mineral percentages, the International Union of Geological Surveying (IUGS) and the QAPF[3] diagram, this rock is classified as

gabbro, although it is marketed as Adelaide black granite. The rock is medium grained and relatively equigranular, with a grain size ranging from 0.02 mm to 6.5 mm, and a dominant crystal size of 2.5 mm. It is fairly homogeneous at the scale of the used specimens with a mass density of 2.95 g cm^{-3}.

Ultrasonic tests provided the P and S-wave velocities of 6.2 km s^{-1} and 3.6 km s^{-1}, respectively, with a variation of less than two percent in the three perpendicular directions, showing very slight material anisotropy. Young's modulus E and Poisson's ratio ν were calculated from ultrasonic velocities and have values $E = 97$ GPa and $\nu = 0.24$. The average Young's modulus and Poisson's ratio obtained from uniaxial compression tests are $E = 102$ GPa and $\nu = 0.24$, which are in good agreement with the ultrasonic data, suggesting only a slight presence micropores or microcracks in the material. The uniaxial compressive strength is $\sigma_c = 180$ MPa and the indirect tensile strength is $\sigma_t = 10.9$ MPa (Bunger et al., 2010).

2.2. Three-point bending testing apparatus

Five different beams were prepared, which were grouped in two beams of small size (height $\times$ span $\times$ thickness) $30.6 \times 102.2 \times 17.3$ and $30.6 \times 102.2 \times 15.9$ mm, two beams of medium size $44.7 \times 153.3 \times 21.6$ and $44.7 \times 153.3 \times 21.4$ mm, and one beam of large size $67.1 \times 230 \times 20.5$ mm, (cf Fig. 1(a)). All beams were fabricated from the same block of Adelaide black gran-

---

³ Q – quartz, A – alkali feldspars, P – plagioclase and F – feldspathoid.

ite and were machined with a sawn notch (1.2 mm wide) in the center position to ease fracture initiation and post-peak control. The height-to-span ratio (D/S) and the notch length to specimen height (a_0/D) were kept constant and equal to, respectively, 0.3 and 0.1.

Fig. 1(c) is a schematic view of the testing apparatus used to load the rock beams in three-point bending. To monitor the evolution of the fracture process zone, sensors for recording the acoustic emission activity were positioned around the notch tip. The three-point bending tests were conducted in a closed-loop, servo-hydraulic load frame with the feedback signal taken as the crack mouth opening displacement (CMOD) across the sawn notch at a gage length of 15 mm. A strain gage-based transducer monitored the CMOD and was programmed to increase it at a rate of 0.05 μm/s. The load applied was recorded with a load cell with a capacity of 22.2 kN. All tests were stopped in the post-peak region after decreasing to 60 % of the peak load.

3. Numerical modelling

The evolution of the fracture process zone was investigated numerically with the aid of a non-local elasto-plasto-damage model for small deformations. Damage models have been successfully employed to model brittle and quasi-brittle non-linear material failure (Havlásek et al., 2016; Cervera et al., 2017; Nguyen et al., 2017). The constitutive model is based on Drucker–Prager plasticity coupled with an isotropic continuum damage description to account for elastic degradation and post-peak softening. Plasticity is defined in the damage-effective stress space, and the damage-driving variable depends on the increase in effective plastic strain. Adding plasticity to the damage mechanism introduces irreversible strains and extends the range of confining pressure in which the constitutive model remains valid (Grassl and Jirásek, 2006; Parisio and Laloui, 2017). The Drucker–Prager model was chosen to avoid over-complications in the constitutive response and therefore to be able to highlight the principal features related to the kinetics of the fracture process zone.

3.1. The plastic model

The stress-strain equation is written in terms of total stress as

$$\boldsymbol{\sigma} = (1 - d)\boldsymbol{E} : (\boldsymbol{\epsilon} - \boldsymbol{\epsilon}^{\mathrm{p}}), \tag{1}$$

where d is the damage internal variable, $\boldsymbol{\epsilon}$ is the total strain tensor, $\boldsymbol{\epsilon}^{\mathrm{p}}$ is the plastic strain tensor and $\boldsymbol{E}$ is the (undamaged) elastic stiffness tensor. Alternatively, the constitutive equation can be written in terms of damage effective stress $\tilde{\boldsymbol{\sigma}}$, i.e., the stress acting on the undamaged part of the material, as

$$\boldsymbol{\sigma} = (1 - d)\tilde{\boldsymbol{\sigma}}. \tag{2}$$

The plastic yield surface is formulated in terms of damage effective stress $f_{\mathrm{p}}(\tilde{\boldsymbol{\sigma}})$ and the Karush–Kuhn–Tucker loading-unloading conditions are

$$f_{\mathrm{p}}(\tilde{\boldsymbol{\sigma}}) \leq 0 \quad \dot{\lambda} \geq 0 \quad \dot{\lambda} f_{\mathrm{p}}(\tilde{\boldsymbol{\sigma}}) = 0. \tag{3}$$

where $\dot{\lambda}$ is the plastic multiplier determining the magnitude of the plastic strain rate

$$\dot{\boldsymbol{\epsilon}}^{\mathrm{p}} = \dot{\lambda} \frac{\partial g_{\mathrm{p}}}{\partial \tilde{\boldsymbol{\sigma}}} \tag{4}$$

whereas its direction is given by the plastic potential gradient in the damage effective stress space. Usually, the associated plasticity overestimates experimental values of dilatancy observed in rocks and soils, motivating the use of non-associated frameworks

(Maier and Hueckel, 1979). The Drucker–Prager plastic yield surface reads

$$f_{\mathrm{p}} = \sqrt{J_2} - \beta I_1 + k = 0, \tag{5}$$

where $I_1 = \mathrm{tr}(\tilde{\boldsymbol{\sigma}})$ is the first invariant of the effective stress tensor and $J_2 = (\tilde{\mathbf{s}} : \tilde{\mathbf{s}})/2$ is the second invariant of the deviatoric effective stress tensor $\tilde{\mathbf{s}}$ defined as

$$\tilde{\mathbf{s}} = \tilde{\boldsymbol{\sigma}} - \frac{1}{3}\mathrm{tr}(\tilde{\boldsymbol{\sigma}})\mathbf{I}. \tag{6}$$

In the current study, we have adopted a regularized expression of g_{p} to maintain differentiability under pure hydrostatic tension conditions

$$g_{\mathrm{p}} = \sqrt{J_2 + \frac{1}{2}\alpha_{\mathrm{p}} I_1^2} - \beta_{\mathrm{p}} I_1 = 0. \tag{7}$$

In Eq. (5), β is the frictional coefficient and k the intercept at zero hydrostatic effective stress, i.e., the cohesive component. In Eq. (7), β_{p} controls dilatancy, whereas α_{p} introduces the smooth tension cap and modifies the dilatancy values under loadings close to hydrostatic tension. For application purposes, especially for brittle materials, the parameters of Eq. (5) can be directly related to the compressive and tensile strength, σ_{c} and σ_{t}, respectively, as

$$\begin{aligned} \beta &= \frac{1}{\sqrt{3}}\left(\frac{\sigma_{\mathrm{c}} - \sigma_{\mathrm{t}}}{\sigma_{\mathrm{t}} + \sigma_{\mathrm{c}}}\right) \\ k &= \frac{2}{\sqrt{3}}\left(\frac{\sigma_{\mathrm{t}}\sigma_{\mathrm{c}}}{\sigma_{\mathrm{t}} + \sigma_{\mathrm{c}}}\right). \end{aligned} \tag{8}$$

In this study, we have used Eq. (8) to obtain the values of parameters β and k from the uniaxial compressive and tensile strengths. Considering that for Adelaide granite, the uniaxial compressive strength is $\sigma_{\mathrm{c}} = 180$ MPa and the indirect tensile strength $\sigma_{\mathrm{t}} = 10.9$ MPa (cf. Section 2), we obtain $\beta = 0.51$ and $k = 11.9$ MPa. Friction and dilatancy coefficients are assumed equal, $\beta = \beta_{\mathrm{p}}$, because of insufficient data on dilatancy. The regularized plastic flow parameter is set to $\alpha_{\mathrm{p}} = 0.10$. Similarly, the yield surface was regularized and rewritten as

$$f_{\mathrm{p}} = \sqrt{J_2 + \frac{1}{2}\delta_{\mathrm{p}} I_1^2} - \beta I_1 + k = 0, \tag{9}$$

with

$$\delta_{\mathrm{p}} = 1 \times 10^{-4}. \tag{10}$$

The regularization of the yield surface leaves the strength envelope unchanged, although it strongly improves convergence of the stress-return algorithm.

3.2. Coupling of the damage internal variable to plastic flow

Damage d is defined as a function of plastic strain by the following expression

$$d = \omega(\bar{k}_d) = (1 - \beta_d)\left[1 - \exp\left(-\frac{\bar{k}_d}{\alpha_d}\right)\right], \tag{11}$$

where α_d and β_d are material parameters and $\bar{k}_d$ is the non-local damage driving variable. The latter is a function of the local damage driving variable k_d which is in turn a function of the plastic effective strain $\epsilon_{\mathrm{eff}}^{\mathrm{p}}$, defined as

$$\epsilon_{\mathrm{eff}}^{\mathrm{p}}(t) = \int_0^t \sqrt{\frac{2}{3}\dot{\boldsymbol{\epsilon}}^{\mathrm{p}} : \dot{\boldsymbol{\epsilon}}^{\mathrm{p}}} \, d\tau. \tag{12}$$

The function that relates the local to the non-local damage driving variable is $\bar{k}_d = f(k_d)$, and its derivation is fully illustrated in

the next section. The evolution equation of the local damage driving variable is written as

$$\dot{k}_d = \frac{1}{\chi_s}\dot{\epsilon}^p_{\text{eff}} \tag{13}$$

where χ_s is a ductility parameter responsible for slowing the evolution of damage at a higher mean confinement

$$\chi_s = \begin{cases} 1 & \text{if } R \leq 1 \\ 1 + h_d(R-1)^2 & \text{if } 1 \leq R \leq 2 \\ 1 - 3h_d + 4h_d\sqrt{R-1} & \text{if } R \geq 2. \end{cases} \tag{14}$$

Here, h_d is a material parameter and R is a ductility measure defined as

$$R = \frac{\sqrt{\tilde{\sigma}:\tilde{\sigma}}}{\sigma_{\text{t}}}. \tag{15}$$

In uniaxial tension, at failure we have $R = 1$, while in uniaxial compression, at failure $R = \sigma_c/\sigma_t$. This can be used directly for the calibration of parameter h_d in Eq. (14).

Eq. (14) is modified from a similar expression presented in Grassl and Jirásek (2006) that was originally developed for concrete to account for the decrease in brittleness with confinement. The additional parameters invoked by the damage formulation are α_d, β_d and h_d. Further discussion about the meaning of the parameters and their calibration can be found in Parisio and Laloui (2017). In our study, β_d is an asymptotic value of damage that is set to 10^{-3}; this helps numerical convergence by assigning a very small (but non-zero) residual stiffness to the elements once damage has fully developed. Since, in the three-point bending tests on single-edge-notched beams, the fracture propagation occurs mainly in tensile mode, we neglect the effects of the confinement and have set $h_d = 0$. Finally, $\alpha_d = 1.7 \times 10^{-3}$ is a measure of the softening rate of the damage model; in our case, it is calibrated to fit the analyses to the load-displacement curve of the small beam.

3.3. Non-local integral averaging

To introduce a micro-structurally motivated internal length scale and to avoid physical inconsistencies related to the pathological mesh-dependent nature of non-regularized softening models, we have employed a non-local integral averaging of the damage driving variable k_d

$$\bar{k}_d(\mathbf{x}) = f(k_d(\mathbf{x})) = \int_V \alpha(\mathbf{x},\boldsymbol{\xi})k_d(\boldsymbol{\xi})\,\mathrm{d}\boldsymbol{\xi}, \tag{16}$$

where α is the normalized weight function expressed as

$$\alpha(\mathbf{x},\boldsymbol{\xi}) = \frac{\alpha_0(\|\mathbf{x}-\boldsymbol{\xi}\|)}{\int_V \alpha_0(\|\mathbf{x}-\boldsymbol{\psi}\|)\,\mathrm{d}\boldsymbol{\psi}}, \tag{17}$$

with the distance measure $r = \|\mathbf{x}-\boldsymbol{\xi}\|$. In the present study, the weight function α_0 is

$$\alpha_0 = \begin{cases} \left(1-\dfrac{r^2}{l_c^2}\right) & \text{if } 0 \leq r \leq l_c, \\ 0 & \text{if } l_c \leq r \end{cases} \tag{18}$$

with l_c referred to as the internal length of the material, or alternatively as the interaction radius (Bažant and Jirásek, 2002). It has the dimension of length and directly controls the long-range interactions in the domain, thus representing the characteristic internal length of the material. The physical meaning underpinning this non-locality of the mechanical behaviour can be related to the presence of heterogeneities of the micro-structure and their long-range (non-local) interactions (Bažant and Jirásek, 2002). Although the internal length has traditionally been treated as a

fixed value, recent efforts have focused on evolving interactions for both integral and gradient-type formulations. Among the proposed solutions, some of the most promising techniques involve stress (Giry et al., 2011) or strain-based (Geers et al., 1998; Saroukhani et al., 2013) modifications of the internal length, alternative integral averages (Grassl et al., 2014), damage-based increasing (Pijaudier-Cabot et al., 2004) and decreasing (Poh and Sun, 2016) interactions, elastic wave propagation (Desmorat et al., 2015), discontinuous fields interpolation (Simone et al., 2003) and a damage-dependent mixed local/non-local formulation (Nguyen, 2011).

Fixed-interaction non-local length models fail to properly capture size effects at the small scale and with variable boundary conditions, such as different ratios of the notch length to the total beam height (Havlásek et al., 2016). In our study, the smaller beam is still in a range in which non-local interaction with a fixed length provides meaningful results, and the ratio of notch depth to beam height is always constant. For the sake of simplicity, to avoid over-parametrization by introducing additional sources of uncertainty into the study and to keep in mind the applicative aim of our contribution, we have chosen in this work to implement a damage model with a fixed internal length, which can still successfully reproduce size effects with fixed geometries and for large enough sizes (Havlásek et al., 2016). This length, being correlated to the micro-structure of the material, was chosen as representative of roughly the extent of the micro-fracture network, as observed by micro-section analysis of fractured specimens (see Fig. 2), i.e., $l_c = 1.25$ mm. The non-local length can alternatively be calibrated by matching both the numerical and experimental total dissipated energy per fracture surface and the standard deviation of the dissipated energy in a numerical setup of uniaxial tension with the standard deviation of the fracture surface roughness obtained from experiments (Xenos et al., 2015).
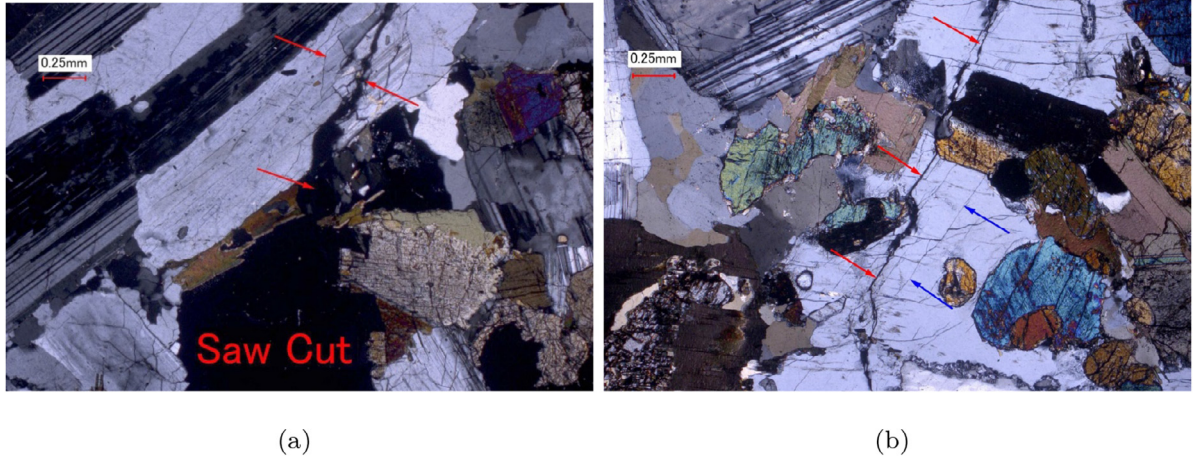
3.4. Numerical implementation and verification

The non-local plastic-damage constitutive model is implemented in the open-source finite element platform OpenGeoSys (Kolditz et al., 2012; Nagel et al., 2016; Parisio et al., 2018). OpenGeoSys is written in object-oriented C++ and allows solving coupled thermo-hydro-mechanical/chemical problems in fractured porous media. The implementation of the constitutive model is fully implicit, with the elasto-plastic effective stress integration being evaluated with a Newton–Raphson algorithm (Nagel et al., 2017), whereas the damage internal variable is evaluated explicitly after convergence of the plastic computation (written in the damage effective stress space). This particularly efficient and robust scheme, which allows for separate solutions for the plasticity and damage problems, is possible because of the framework chosen for coupling damage and plasticity. As the plastic state variable, k_d is evaluated explicitly, and no iterations are necessary to compute the non-local variable $\bar{k}_d$ (Jirásek and Marfia, 2005).

For better efficiency of the numerical algorithm, the effective stress field and yield condition are normalized, and plastic strain is split into deviatoric and volumetric components. This allows the formulation of the 15-dimensional residual vector

$$\mathbf{r}_1 = \frac{\tilde{\sigma}}{G} - 2(\boldsymbol{\epsilon}^D - \boldsymbol{\epsilon}_p^D) - \frac{K}{G}(\epsilon^V - \epsilon_p^V)\mathbf{I} \tag{19}$$

$$\mathbf{r}_2 = \dot{\boldsymbol{\epsilon}}_p^D - \dot{\lambda}\left[\frac{\partial g_p}{\partial\tilde{\sigma}}\right]^D \tag{20}$$

$$r_3 = \dot{\epsilon}_p^V - \dot{\lambda}\left[\frac{\partial g_p}{\partial\tilde{\sigma}}\right]^S:\mathbf{I} \tag{21}$$

Fig. 2. Microphotographs of thin sections of Adelaide black granite under transmitted cross-polarized light. (a) View near the top surface of the sample showing the saw cut (notch) and micro-cracks (red arrows) propagating from it. (b) A view deeper in the sample showing the micro-cracks (red arrows) following cleavage planes (blue arrows) and propagating through grains and along grain boundaries. (For interpretation of the references to colour in this figure legend, the reader is referred to the web version of this article.)

$$r_4 = \dot{\epsilon}_p^{\text{eff}} - \sqrt{\frac{2}{3}\dot{\lambda}^2 \left[\frac{\partial g_p}{\partial \tilde{\sigma}}\right]^D : \left[\frac{\partial g_p}{\partial \tilde{\sigma}}\right]^D} \tag{22}$$

$$r_5 = \frac{f_p}{G}, \tag{23}$$

where $(\bullet)^D$ indicates the deviatoric part of a tensor (cf. Eq. (6)), $(\bullet)^S$ is its spherical part and $\epsilon^V = \epsilon^S : \mathbf{I}$ is a volumetric strain measure. It would be sufficient to solve for either effective stress or plastic strain alone, but instead, we have implemented the stress return by solving the plastic strain and effective stress simultaneously. Doing so allows direct extensions towards non-linearity in elastic parameters, yield surfaces, and hardening laws, depending on both stresses and plastic strains.

The numerical algorithm for the plastic problem consists of finding the solution $\mathbf{r} = \mathbf{0}$ of this residual vector at time step $t + \Delta t$ with respect to the state variables conveniently collected in the vector $\mathbf{z} = \left\{\tilde{\sigma}/G, \epsilon_p^D, \epsilon_p^V, \epsilon_p^{\text{eff}}, \lambda\right\}^T$. Linearization of the residual $\mathbf{r}$ leads to the Newton–Raphson algorithm

$$\mathbf{z}_{n+1}^{t+\Delta t} = \mathbf{z}_n^{t+\Delta t} - \left(\mathbf{J}_n^{t+\Delta t}\right)^{-1} \mathbf{r}_n^{t+\Delta t}, \tag{24}$$

with the Jacobian

$$\mathbf{J}_n^{t+\Delta t} = \left.\frac{\partial \mathbf{r}^{t+\Delta t}}{\partial \mathbf{z}^{t+\Delta t}}\right|_n, \tag{25}$$

where convergence is reached when $\|\mathbf{r}\| < \theta_{\text{tol}}$. The consistent tangent operator $\mathbf{C}_{\text{pl}}$ required for the Newton–Raphson iterations of the global displacement problem can be obtained directly from the components of the Jacobian matrix as

$$\frac{d\mathbf{z}}{d\boldsymbol{\epsilon}} = -\mathbf{J}^{-1}\frac{\partial \mathbf{r}}{\partial \boldsymbol{\epsilon}}, \tag{26}$$

where the first components of the solution vector are the stress components $\tilde{\sigma}/G$ (Nagel et al., 2017).

The finite element approximation of the non-local variable $\bar{k}_d$ is computed explicitly once the plastic stress return algorithm has reached convergence as

$$\bar{k}_{d,i} = \frac{\sum_{j=1}^{n_p} w_j \alpha_0\left(\|\mathbf{x}_i - \mathbf{x}_j\|\right) k_d\left(\mathbf{x}_j\right) \det J(\mathbf{x}_j)}{\sum_{k=1}^{n_p} w_k \alpha_0\left(\|\mathbf{x}_i - \mathbf{x}_k\|\right) \det J(\mathbf{x}_k)} \tag{27}$$

in which n_p represents the number of integration points of the finite element discretization, $\det J(\mathbf{x}_k)$ is the determinant of the Jacobian of the isoparametric transformation. Damage can be evaluated explicitly from Eq. (11) once $\bar{k}_{d,i}$ is known.

Table 1
Model parameters representing Adelaide black granite employed for the numerical simulations.

Parameter	Value	Unit
β	0.51	–
k	11.9	MPa
β_d	1.0×10^{-3}	–
α_d	1.7×10^{-3}	–
h_d	0.0	–
l_c	1.25	mm

3.5. Numerical simulations set-up

Finite element models of the different-sized beams were set up in a two-dimensional plane-stress framework. Because the two small- and two medium-sized beams are of slightly different thicknesses, the results of the numerical models of the beams were normalized to an average thickness of 16.4 mm for the small beam and 21.5 mm for the medium one. The beams were simply supported and the loading was applied via an imposed vertical displacement at a point situated on the top surface, at mid-span of the beams. The parameters employed for the numerical simulations are illustrated in Table 1. Only parameter α_d has been estimated by manual fitting to the smallest beam results, so that simulations can be considered as semi-blind predictions. For all models, first-order quad meshes were employed, with 7002 elements for the small beam, 10, 292 elements for the medium beam and 12, 008 elements for the large beam. The mesh is built such that the largest element within the damage zone is four times smaller than the internal length, to guarantee the accuracy of the non-local damage field. The convergence of the non-linear solver is based on the L_2-norm of the solution update in a time iteration with an absolute tolerance of 10^{-6} and the Sparse LU linear solver from the Eigen library (http://eigen.tuxfamily.org) was employed, with scaling to balance row and column norms for the LU factorization.

4. Configurational mechanics

Linear elastic fracture mechanics is often an inappropriate framework to interpret complex field quantities (stress, strain, damage, plastic strain etc.) that originate from non-local inelastic

computations. We have instead employed the concept of configurational forces to condense the information from the large number of variables, to better interpret the numerical results in the fracture process zone and to address a wider range of problem classes.

Configurational forces, also called material forces, arise from the description of the continuum with respect to an evolving material configuration; in comparison, the classical continuum motion problem usually rests on the description of an evolving spatial configuration under the action of physical forces. In this sense, a change in the configuration of the material points is associated with a change in energy, and configurational forces can be seen as the reactions offered by the material in response to a configurational change of its material points (Maugin, 1995; Gross et al., 2003; Mueller et al., 2004; Maugin, 2016). Configurational mechanics is a powerful and versatile tool to study evolving discontinuities, such as phase transitions, inhomogeneities, cracks, voids, inclusions, boundaries but also discretization accuracy in finite element applications and non-trivial mechanical systems (Maugin, 1998; Gross et al., 2003; Mueller et al., 2004; Gurtin, 2008; Li and Wang, 2008; Nagel and Kelly, 2012; Bigoni et al., 2014; Kuhn et al., 2015; Maugin, 2016; Parisio et al., 2018). Such considerations proceed from a total potential or a material momentum balance and commonly lead to the appearance of the energy momentum tensor (also called the Eshelby stress tensor).

4.1. Thermodynamic derivation of configurational forces

We introduce the concept of configurational forces loosely following our previous work on the topic (Parisio et al., 2018). To differentiate between spatial and material operators, those starting with capital letters—i.e., $\mathrm{Grad}(\bullet)$ and $\mathrm{Div}(\bullet)$—represent differential operators with respect to material coordinates $\mathbf{X}$ and those starting with lower-case letters—i.e., $\mathrm{grad}(\bullet)$ and $\mathrm{div}(\bullet)$—are relative to spatial coordinates $\mathbf{x}$.

The Helmholtz free energy density $\psi(\mathbf{F}, \boldsymbol{\kappa}, \kappa; \mathbf{X})$ is postulated in an isothermal setting as a function of the deformation gradient $\mathbf{F}$, internal variables $\boldsymbol{\kappa}$ and κ and the material coordinates $\mathbf{X}$. The Clausius–Planck inequality can then be expanded to

$$\left(\mathbf{P} - \frac{\partial \psi}{\partial \mathbf{F}}\right) : \dot{\mathbf{F}} - \frac{\partial \psi}{\partial \boldsymbol{\kappa}} : \dot{\boldsymbol{\kappa}} - \frac{\partial \psi}{\partial \kappa} \dot{\kappa} \geq 0, \tag{28}$$

where $\mathbf{P}$ is the first Piola–Kirchhoff stress tensor and the constitutive relations

$$\mathbf{Y}_{\boldsymbol{\kappa}} = -\frac{\partial \psi}{\partial \boldsymbol{\kappa}}; \; Y_{\kappa} = -\frac{\partial \psi}{\partial \kappa}; \; \mathbf{P} = \frac{\partial \psi}{\partial \mathbf{F}} \tag{29}$$

with $\mathbf{Y}_{\boldsymbol{\kappa}}$ and Y_{κ} defined as the associated thermodynamic variables (or thermodynamic forces) to the internal variables $\boldsymbol{\kappa}$ and κ. The resulting mechanical dissipation inequality reads

$$\mathcal{D}_{\mathrm{M}} = \mathbf{Y}_{\boldsymbol{\kappa}} : \dot{\boldsymbol{\kappa}} + Y_{\kappa} \dot{\kappa} \geq 0, \tag{30}$$

The second law of thermodynamics implies that the total dissipation, which is the sum of the mechanical and thermal dissipation, must be non-negative. The thermal dissipation remains implicit in our isothermal treatment and is assumed to be much smaller than the mechanical dissipation. This implies that the mechanical dissipation $\mathcal{D}_{\mathrm{M}}$ itself must be positive (Houlsby and Puzrin, 2007), which is a more stringent interpretation than the second law of thermodynamics.

The gradient of the Helmholtz free energy density

$$\mathrm{Grad}\,\psi = \frac{\partial \psi}{\partial \mathbf{F}} : \mathrm{Grad}\,\mathbf{F} + \frac{\partial \psi}{\partial \boldsymbol{\kappa}} : \mathrm{Grad}\,\boldsymbol{\kappa} + \frac{\partial \psi}{\partial \kappa} \mathrm{Grad}\,\kappa + \frac{\partial \psi}{\partial \mathbf{X}}\bigg|_{\mathrm{expl.}} \tag{31}$$

can be transformed by applying Young's theorem to

$$\mathbf{0} = \mathrm{Div}\,(\psi \mathbf{I} - \mathbf{F}^{\mathrm{T}} \mathbf{P}) + \mathbf{F}^{\mathrm{T}} \mathrm{Div}\,\mathbf{P} + \tag{32}$$

$$+ \mathbf{Y}_{\boldsymbol{\kappa}} : \mathrm{Grad}\,\boldsymbol{\kappa} + Y_{\kappa}\,\mathrm{Grad}\,\kappa - \frac{\partial \psi}{\partial \mathbf{X}}\bigg|_{\mathrm{expl.}}$$

The balance equation of configurational forces can be obtained by inserting the Eshelby stress tensor defined as $\boldsymbol{\Sigma} = \psi \mathbf{I} - \mathbf{F}^{\mathrm{T}} \mathbf{P}$, and the balance of linear momentum $\mathrm{Div}\,\mathbf{P} + \rho_0 \mathbf{b} = \mathbf{0}$, into Eq. (32), resulting in

$$\mathbf{0} = \mathrm{Div}\,\boldsymbol{\Sigma} + \mathbf{g}, \tag{33}$$

with the configurational body forces

$$\mathbf{g} = \mathbf{g}_{\mathrm{diss}} + \mathbf{g}_{\mathrm{vol}} + \mathbf{g}_{\mathrm{inh}}, \tag{34}$$

consisting of the three contributions

$$\mathbf{g}_{\mathrm{diss}} = \mathbf{Y}_{\boldsymbol{\kappa}} : \mathrm{Grad}\,\boldsymbol{\kappa} + Y_{\kappa}\,\mathrm{Grad}\,\kappa$$
$$\mathbf{g}_{\mathrm{vol}} = -\rho_0 \mathbf{F}^{\mathrm{T}} \mathbf{b} \tag{35}$$
$$\mathbf{g}_{\mathrm{inh}} = -\frac{\partial \psi}{\partial \mathbf{X}}\bigg|_{\mathrm{expl.}},$$

where $\mathbf{b}$ is the vector of physical body forces. In Eq. (34), the components of the total configurational forces are divided into contributions due to heterogeneities created by dissipative phenomena $\mathbf{g}_{\mathrm{diss}}$, deformations or rotations in the presence of body-forces $\mathbf{g}_{\mathrm{vol}}$ and material inhomogeneities $\mathbf{g}_{\mathrm{inh}}$.

The Eshelby stress in the present small-strain framework is defined as

$$\boldsymbol{\Sigma} = \psi \mathbf{I} - \mathrm{grad}^{\mathrm{T}} \mathbf{u}\,\boldsymbol{\sigma}, \tag{36}$$

with $\boldsymbol{\sigma}$ being Cauchy's stress tensor and $\mathrm{grad}^{\mathrm{T}} \mathbf{u}$ being the transposed displacement gradient. The volumetric component of configurational forces simplifies to

$$\mathbf{g}_{\mathrm{vol}} = -\varrho\,\mathrm{grad}^{\mathrm{T}} \mathbf{u}\,\mathbf{b}. \tag{37}$$

Parisio et al. (2018) carried out an implementation of the configurational forces in the finite element software OpenGeoSys; see this work for additional details and a comparison against an analytical solution for a problem of moving internal boundaries.
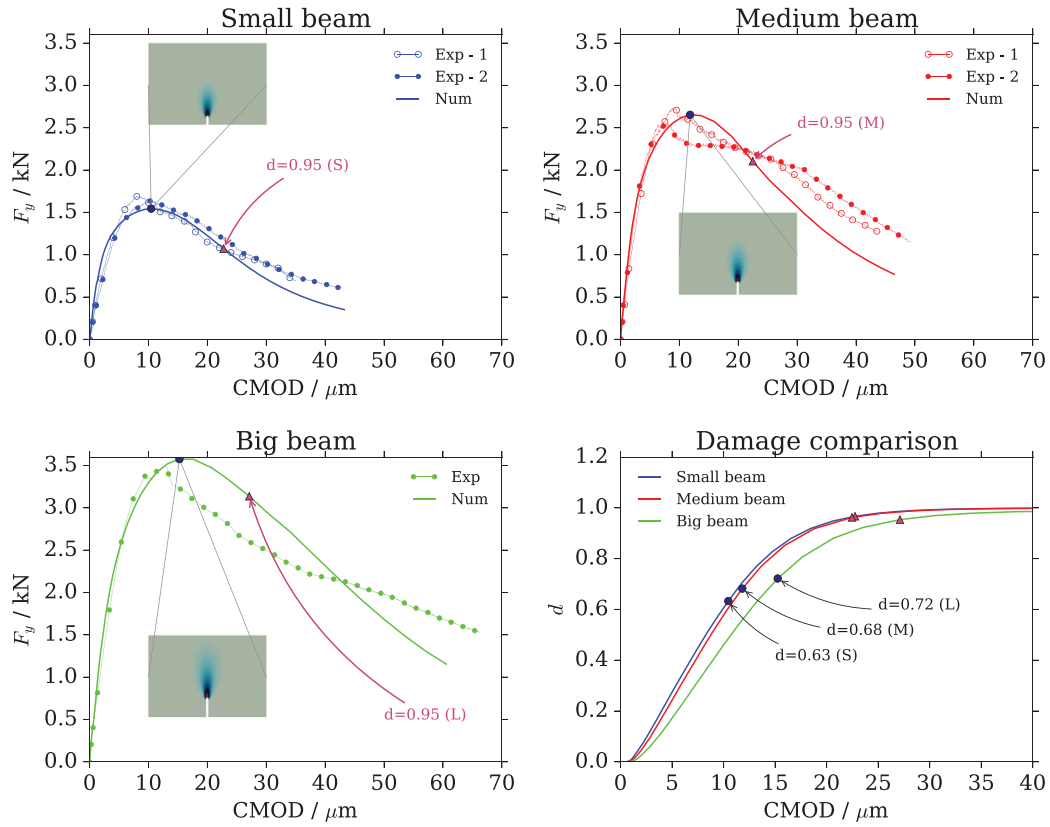
5. Results

5.1. Micro-structure

Fig. 2 reports two microscopic analyses of thin sections of a failed granite beam under cross-polarized light around the notch, Fig. 2(a), and deeper in the specimen, Fig. 2(b). As shown in the first image, the crack propagates from the notch, as expected, and a clearly visible network of micro-cracks tends to follow the cleavage planes in the plagioclase. This image shows that the inelastic processes of the fracture process zone indeed happen at the grain level, and multiple fracture paths can be observed in a finite-sized area. The second micro-image highlights the tendency of micro-cracks to originate at and develop along grain boundaries, where the local shear concentration is caused by differences in stiffness and strength.

5.2. Global behaviour

In Fig. 3, we present the results of the experiments and simulations in terms of the applied vertical force against the CMOD. The plot shows good agreement between the curves obtained experimentally and those from the finite element simulations. Because of the constitutive formulation, damage evolves with effective plastic strain so that the extent of the damaged zone corresponds to the locations in which inelastic dissipation takes place: It can be assumed it coincides with the fracture process zone. Considering that the rock behaves as a brittle material and within the framework of

Fig. 3. Comparison between experimental and numerical results in terms of axial load versus crack mouth opening displacements (CMOD) for the three beams under investigation. The dotted curves represent the experimental results, and the solid lines are from the numerical analyses. Below the curves, a contour plot of the damage field at the force peak computed from finite element analyses, is shown (the relative scale of the beam sizes is maintained). The damage evolution at the crack mouth obtained from the numerical model is shown in the last image for the three beams under study. Damage is shown at force peak for the three beams and when it has reached $d = 0.95$. This result highlights the different rates at which a crack fully propagates and how this rate depends on the beam size. At larger structural sizes, the two points in the damage curve become closer, implying more brittleness, and the solutions are closer to those based on linear elastic fracture mechanics theory.

linear elastic fracture mechanics, a cohesionless crack should not exist prior to peak load, when crack initiation occurs. However, if the size of the process zone is comparable to the specimen size, a cohesionless crack might exist at the peak load. Recent experimental evidence has shown the possibility of crack propagation prior to the peak load (Fakhimi et al., 2017).

If the crack is static at the peak vertical force, the fracture process zone is still evolving and not at its full extent. This is shown in the damage comparison, with the values of damage at peak and when it reaches $d = 0.95$, which is arbitrarily assumed in this case as the value for crack propagation. It is possible to observe that damage at force peak increases with beam size. Furthermore, the greater the damage at force peak the faster it will reach $d = 0.95$, i.e., a fully damaged condition, implying more brittleness. Ideally, when the beam is large enough, asymptotic conditions will be reached in which damage in the notch at force peak will tend toward $d = 1.0$, with the behaviour ideally predicted by the linear elastic fracture mechanics for large structural sizes relative to the fracture process zone.

5.3. Size effects

From the theory of elastic-brittle beams, the nominal strength[4] of geometrically similar beams σ_N can be expressed as

$$\sigma_N = \frac{3}{2} \frac{FL}{bD^2},\tag{38}$$

---

[4] The nominal strength is the equivalent to the stress value in elastic beam theory, occurring at the fibre with the highest solicitation in tension at the failure load.

where F is the maximum vertical force, L is the beam support span, b is its width and D is its height. In the theory of nonlinear fracture mechanics, σ_N is bounded between the asymptotic solutions of size-independent plasticity at small sizes and linear elastic fracture mechanics as $\sigma_N \propto \sqrt{D}$ at higher dimensions. In a $(\log D, \log \sigma_N)$ plane, the strength-size law predicted by linear elastic fracture mechanics is a straight line with slope $-1/2$.

Fig. 4 plots the nominal strength as a function of the beam height D for the experimental data (blue triangles) and for the numerical results (red circles). There is fair agreement between experimental data and numerical predictions, although the plastic limit at small sizes obtained from the numerical analyses seems to underestimate the available strength. This could be related to the fact that our predictions are based on tensile strength values measured in Brazilian tests, which may themselves be affected by size dependency and may be too far from the plastic limit. To take into account the non-linear effects and dissipation caused by plasticity and micro-cracking in the fracture process zone, Bažant (1984) introduced the following expression of nominal strength

$$\sigma_N = \frac{B\sigma_t}{\sqrt{1 + \frac{D}{D_0}}},\tag{39}$$

where σ_t is the tensile strength, B is a geometry factor and D_0 is the transition size between the two asymptotic solutions of size-independent strength (plastic theory) and size dependency as predicted by linear elastic fracture mechanics. To build the size effect curves for the experimental and numerical data, we have employed the least squares method to fit the values D and σ_N in Eq. (39),
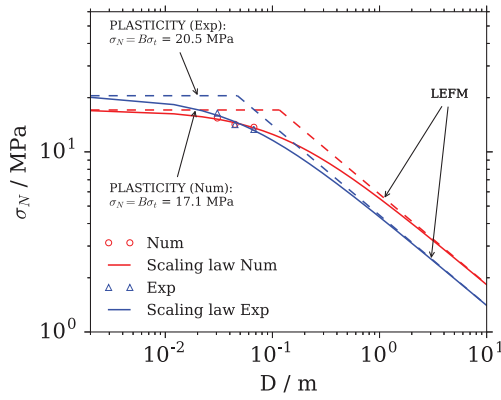
Fig. 4. The comparison is satisfactory between experimental measurements and numerical predictions of size effects in terms of the dependence of nominal strength σ_N on structural size D. This result demonstrates de facto that non-linear local analyses are necessary for analysis of the present set of tests because the beam sizes of Adelaide granite are located in the transition zone between size-independent plasticity and the theory of linear elastic fracture mechanics. (For interpretation of the references to colour in this figure legend, the reader is referred to the web version of this article.)

obtaining $B\sigma_t = 20.5$ MPa and $D_0 = 0.047$ m for the experimental data and $B\sigma_t = 17.1$ MPa and $D_0 = 0.116$ m for the numerical data. Fig. 4 shows experimental and numerical scaling laws of nominal strength, highlighting the two asymptotic solutions for large and small sizes. The plot clearly illustrates that the specimens under investigation are situated in the transition zone, in which neither plastic theory nor linear elastic fracture mechanics would lead to correct predictions. Extrapolation of the results to other sizes has to be handled with particular care: small discrepancies between experiments and predictions at the decimeter scale can be amplified at larger structural sizes. Furthermore, at the smaller size in the end of the curve, the actual size of the structure becomes comparable to the grain size, and the hypothesis of a homogeneous continuum may no longer be valid.

5.4. Damage and acoustic emissions

Fig. 5 shows the distribution of acoustic emission events from the experimental analyses and damage from the numerical analyses in the mid-sized beam and at different load steps, which are taken at given values of the ratio between the post-peak load to the peak load in the experimental curve. The time instants in the numerical analyses are taken to have the CMOD as close as possible to the experimental value, which means that the load ratio indicated might be slightly different for the numerical analyses. As damage and acoustic emissions are representative of the inelastic dissipative phenomena (Grẽgoire et al., 2015), they can both be employed to identify the fracture process zone evolution and to compare experimental results to numerical predictions in a local manner. The numerical model captures the increasing extent of the fracture process zone well. Aside from the global validation presented in the previous paragraph, this result provides strong support that the local evolution of the fracture process zone is captured by the model in a realistic manner.

The data on acoustic emissions indicate that micro-cracks start to nucleate from the notch and the boundaries of the model (Lockner et al., 1991) and then later propagate toward the middle of the sample, which is well reproduced by the computed damage distribution. The number of acoustic emission events dramatically increases from 90% to 80% of the peak load. The damage distribution obtained from finite element analyses is also in good agreement with the distribution of acoustic emission events, which is

to be read as a meaningful representation of the local response in terms of dimension of the area subjected to inelastic dissipation.

Concerning the extent of the fracture process zone, Fig. 6 presents a direct comparison between recorded acoustic emission events during the experimental procedure and the damage distribution obtained from the numerical analyses. Once again, the beam under investigation is the mid-sized one. Acoustic emission data have been processed as follows: first, the discretized distribution of events that was recorded until a given time instant and along a particular direction (either x or y) is computed; second, the distribution is normalized against its maximum; third, to make a direct comparison with damage, the entire distribution is scaled multiplicatively by the maximum value that numerical damage has reached along that direction and at that specific instant. In this way, the plots obtained for acoustic emission data are to be read qualitatively, and they serve the purpose of establishing the extent of the zone in which the inelastic process took place. In other words, this method of computing the normalized and scaled distribution gives an indication of the extent of the fracture process zone from the experimental measurements, which can be directly compared against the non-locally computed damage (although it should not be read as an accurate numerical value of the damage). Along the vertical direction, the size of the damaged zone increases during loading, whereas in the horizontal direction, the size increment is negligible. The numerical predictions agree well with the experimental results in both directions. An additional discrepancy is observed in the vertical direction: as deformation progresses, the computed damage extends over a larger area than the acoustic emission distribution. Hence, our computations predict higher damage values in the post-peak phase than what are actually observed. This can also be observed in the global load-displacement curve for the medium beam, which softens more rapidly than the experimental curve. Despite this minor discrepancy, the size of the fracture process zone and its rate of increase are generally well reproduced by the numerical analyses. The methodology for assessing the value of internal length, which is based on thin-section analyses of the fractured area, is also considered to be validated for this particular application.

5.5. Fracture energy and configurational mechanics

In this section we have investigated the size dependency by using a classical linear elastic fracture mechanics approach and have compared it with the enhanced information that can be retrieved with configurational mechanics arguments. Linear elastic fracture mechanics inaccurately predict toughness and fracture energy when the fracture process zone is non-negligible.

The energy release rate G equals the negative change of potential energy in the solid and is computed as

$$G = -\frac{\partial \Pi}{\partial A} = \frac{K_I^2}{E}, \tag{40}$$

where A is the crack area and K_I is mode-I fracture toughness, which, for notched beams, can be expressed as (Guinea et al., 1998)
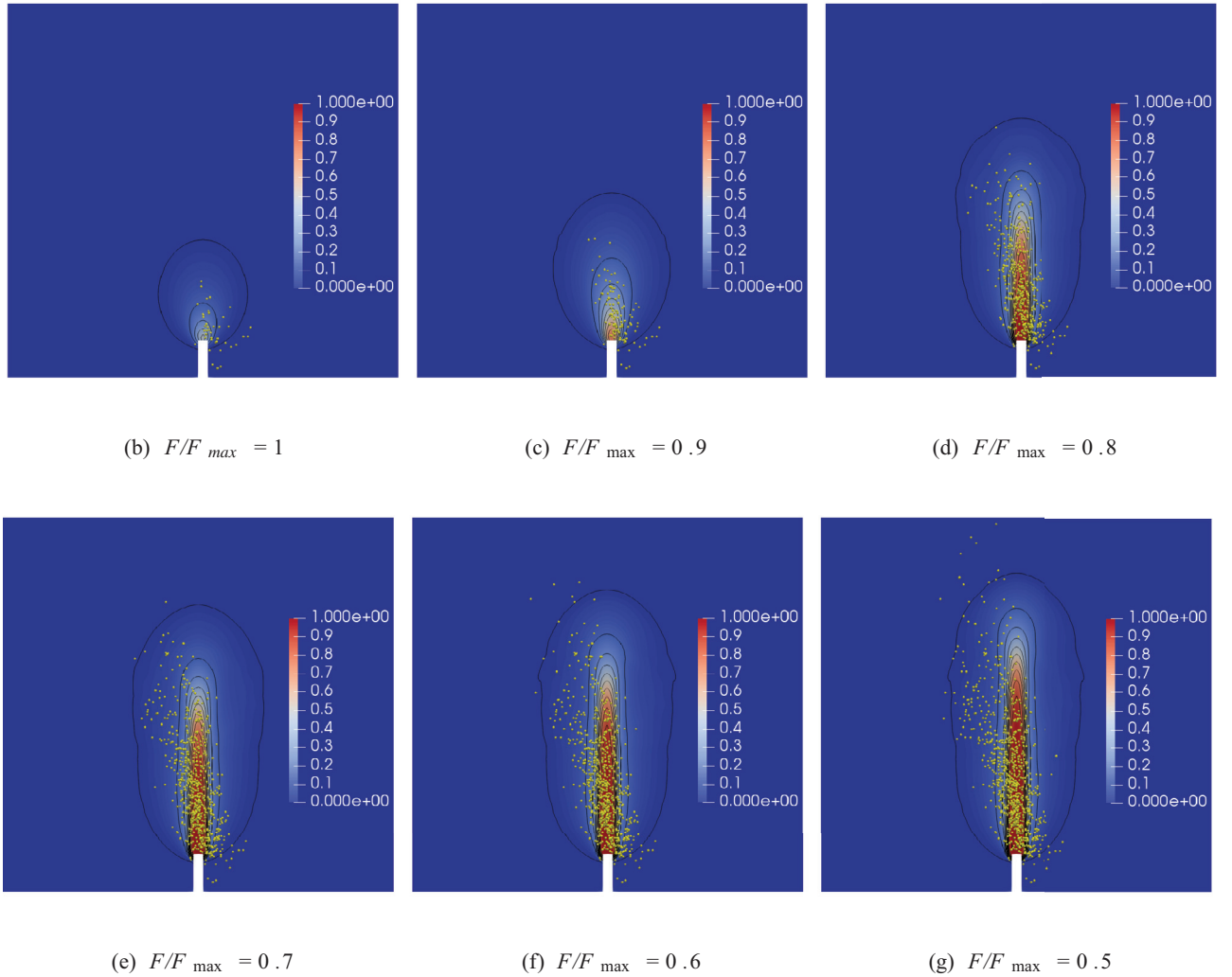
$$K_I = \sigma_N f_I(\theta, \delta)\sqrt{D}, \tag{41}$$

with $f_I(\theta, \delta)$ being a mode-I shape factor that depends on the beam depth-to-notch ratio $\theta = D/a$ and span-to-depth ratio $\delta = S/D$, written as

$$f_I(\theta, \delta) = \frac{\sqrt{\theta}}{(1-\theta)^{3/2}(1+3\theta)}\left\{p_\infty(\theta) + \frac{4}{\delta}[p_4(\theta) - p_\infty(\theta)]\right\}. \tag{42}$$
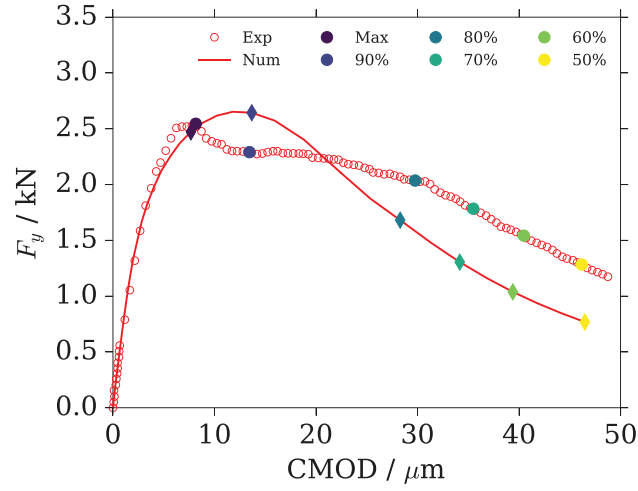
(a) Points location of cumulative acoustic emission plots in the load-displacement curve

(b) $F/F_{max} = 1$

(c) $F/F_{max} = 0.9$

(d) $F/F_{max} = 0.8$

(e) $F/F_{max} = 0.7$

(f) $F/F_{max} = 0.6$

(g) $F/F_{max} = 0.5$

Fig. 5. Comparison of numerical and experimental results in terms of acoustic emissions and damage contour for the medium beam (Experiment 2). The kinematics and size of the fracture process zone are compared in terms of acoustic emissions events (dots) obtained during experimental testing and damage contour plot for the numerical FE analyses at CMODs corresponding to the peak load and post-peak at 90%, 80%, 70% 60% and 50% of the peak load (referring to the experimental data).
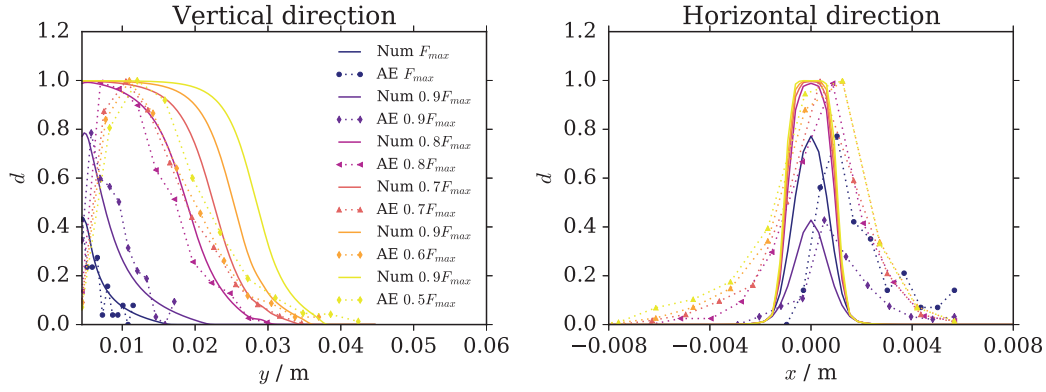
Fig. 6. Comparison between damage and acoustic emission distribution along vertical (parallel to the crack plane) and horizontal (perpendicular to the crack plane) lines for the mid-sized beam (Experiment 2) from peak load into post-peak. The distribution of damage is obtained directly from the numerical analyses.

The cubic polynomial $p_\delta(\theta)$ for $\delta = 4$ and for pure bending ($\delta = \infty$) are

$$p_4(\theta) = 1.9 + 0.41\theta + 0.51\theta^2 - 0.17\theta^3$$
$$p_\infty(\theta) = 1.99 + 0.83\theta - 0.31\theta^2 + 0.14\theta^3. \tag{43}$$

Configurational forces can be employed to assess the fracture energy release rate from a local approach that takes into account the fracture process zone at the crack-tip. Rice's J-integral (Rice, 1968) represents the negative rate of change of potential energy due to crack propagation (cf. Eq. (40)) and can be written in a generalized three-dimensional form[5]:

$$\mathbf{J} = \int_\Gamma \mathbf{\Sigma N} d\Gamma, \tag{44}$$

where the Eshelby stress tensor introduced previously has been used and where Γ is an arbitrary contour that encloses the crack-tip. The J-integral is equal to the crack energy release rate for planar crack growth, and according to Eshelby's theory (Eshelby, 1951), the (configurational) force on a defect $\mathbf{G}^{\text{inh}}$ is the negative rate of increase in the total potential energy upon translation of the defect (Li and Wang, 2008)

$$\delta\Pi = -\mathbf{G}^{\text{inh}} \cdot \delta\mathbf{X} = \frac{\partial\Pi}{\partial\mathbf{X}} \cdot \delta\mathbf{X}. \tag{45}$$

To demonstrate the connection between the J-integral, material forces and the energy release rate in a simple manner, consider a coordinate system $\{\mathbf{E}_i\}$ aligned with the crack plane such that self-similar crack growth occurs parallel to the $\mathbf{E}_1$-direction in a planar fashion with the crack surface normal direction $\mathbf{E}_2$ and is homogeneous along the thickness direction $\mathbf{E}_3$ with the thickness B. Then,

$$\delta\mathbf{X} = \delta a\mathbf{E}_1, \quad \delta\mathbf{\Gamma} = B\mathbf{E}_3 \times \delta\mathbf{X} = B\delta a\mathbf{E}_2 = \delta A\mathbf{E}_2, \tag{46}$$

and

$$\delta\Pi = -\mathbf{G}^{\text{inh}} \cdot \mathbf{E}_1\delta a = -\frac{1}{B}\mathbf{G}^{\text{inh}} \cdot \mathbf{E}_1\delta A. \tag{47}$$

By comparison with Eq. (40) we observe that the energy release rate follows from the material force field via $G = \mathbf{G}^{\text{inh}} \cdot \mathbf{E}_1/B$. With the relationship between material forces and energy release rate established, the relationship to the J-integral defined in Eq. (44) becomes apparent in conjunction with Eqs. (33) and (36).

Configurational forces can be directly employed to calculate the local crack energy release rate. We have computed the sum of the vertical components of configurational forces ahead of the crack

Table 2
Critical energy release rate comparison G_c (values are in Pa $\cdot$ m) between experimental and numerical values with the four different methods: I) toughness-experimental, II) toughness-numerical III) corrected toughness-numerical and IV) configurational forces-numerical. The last two entries indicate the ratios between different methods.

Method	I	II	III	IV	IV/I	IV/II
Small beam	24.4	21.3	44.5	48.7	1.93	2.29
Medium beam	26.5	26.5	47.2	51.6	1.95	1.95
Big beam	35.5	37.1	62.7	60.2	1.70	1.62

tip to obtain the energy release rate from local measurements. These are compared with the values computed as a function of the toughness, which is estimated by employing the theory of single-edge-notch three-point bending beams. The values for energy release rate computed from experimental and numerical results for the three beams are reported in Table 2. The numerical results are further computed by employing three distinct methodologies, so that, in total, four methods are used:
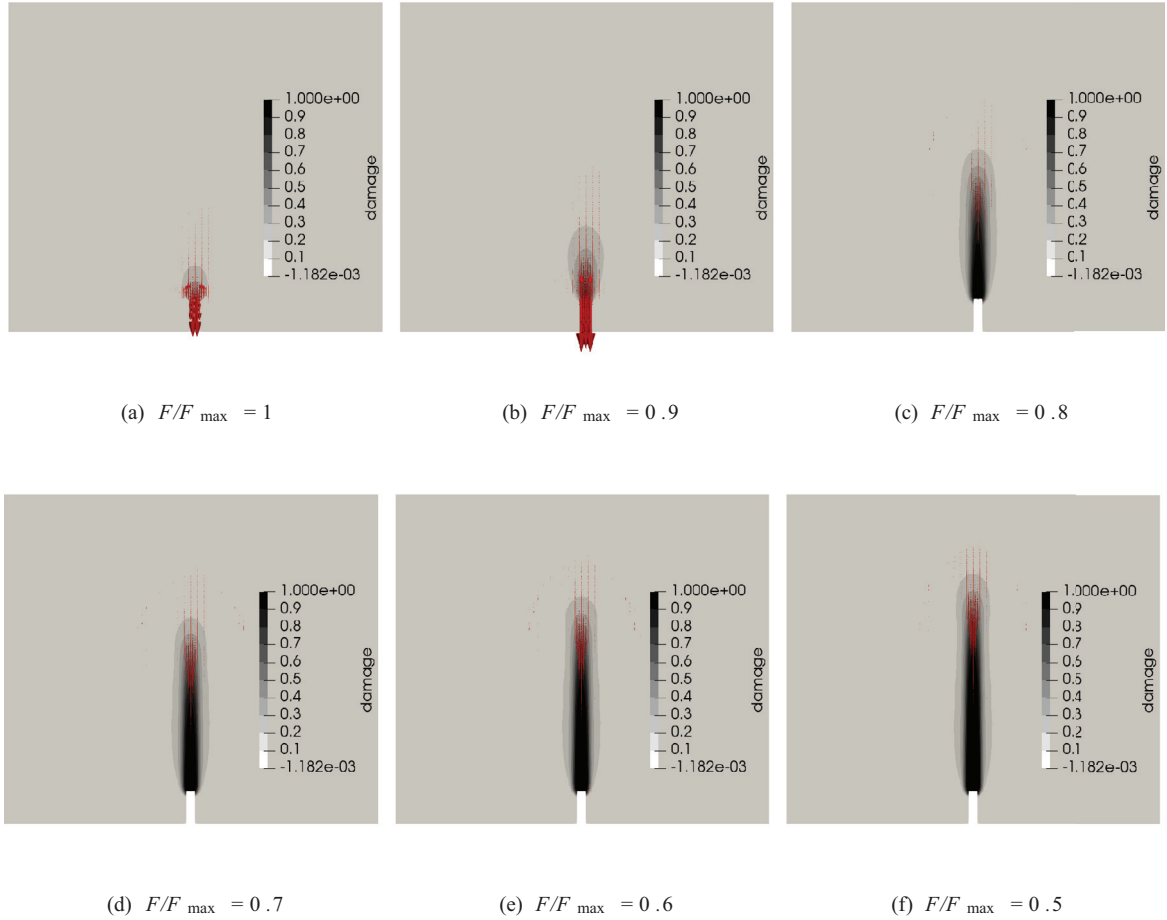
- Method I - $G_c = K_{\text{Ic}}^2/E$, where toughness is computed from Eq. (41) with σ_N taken from *experimental* results;
- Method II - $G_c = K_{\text{Ic}}^2/E$, where toughness is computed from Eq. (41) with σ_N taken from *numerical* results;
- Method III - $G_c = [K_{\text{Ic}}(a^{\text{eff}})]^2/E$, where toughness is computed from Eq. (41) with values of σ_N^* taken from *numerical* results and the values account for a *fracture process zone corrected notch depth* a^{eff} from Eq. (49) (explained below);
- Method IV - $G_c = \mathbf{G}^{\text{inh}} \cdot \mathbf{E}_1/B$, i.e., from configurational forces.

The *notch-length correction* is a method used to extend the validity of linear elastic fracture mechanics by accounting for crack-tip stress-shielding caused by dissipative effects ahead of the crack tip. In standard linear elastic fracture mechanics, the fracture process zone is considered significantly smaller than the K-dominated zone given by the elastic solution. In contrast, ductile materials generally have a plastic zone that encloses the smaller fracture process zone. In between both cases, some materials satisfy the assumption of small-scale yielding which implies that the plastic zone also remains small in comparison to the K-dominated region and its extent is determined by the stress-intensity factor as well as the yield limit of the material. A first approximation for the extent of the plastic zone can be found by a simple shift of the elastic solution and is given for plane-stress conditions as

$$r_p = \frac{1}{2\pi}\left(\frac{K_I}{\sigma_t}\right)^2. \tag{48}$$

---

[5] The scalar J-integral follows from the projection along a crack-growth direction, classically in a two-dimensional setting.

(a) $F/F_{max} = 1$

(b) $F/F_{max} = 0.9$

(c) $F/F_{max} = 0.8$

(d) $F/F_{max} = 0.7$

(e) $F/F_{max} = 0.6$

(f) $F/F_{max} = 0.5$

Fig. 7. Damage field and vertical component of configurational forces for the medium beam at the peak and in the post-peak branch at 90%, 80%, 70% 60% and 50% of the peak load (referring to the experimental data).

Equilibrium considerations correcting for plastic effects show that to maintain static equilibrium in the presence of lowered stress-transfer across the ligament, the extent of the plastic zone is larger, i.e., $l_p = 2r_p$. Under these assumptions of small-scale yielding, Irwin's effective crack length reads

$$a^{\text{eff}} = a + r_p \tag{49}$$

and can be used to characterize the stress-field outside the plastic zone by means of a corrected stress-intensity K^{eff}. This is done in Method III.

The results of this computation highlight once more the presence of the fracture process zone in terms of dissipation energy. The energy release rate computed from the maximum load assumes the validity of linear elastic fracture mechanics, for which energy is dissipated uniquely in the process of creating two new free surfaces. In reality, plastic processes and micro-cracking ahead of the crack tip dissipate energy as well, so the energy required to propagate the fracture is the sum of the two contributions (surface creation + crack-tip inelasticity). This is highlighted well in the results obtained from the configurational forces: The energy release rate computed locally takes into account the crack-tip plastic processes (excluded in the global approach), resulting in a higher energy release rate than that predicted by linear elastic fracture mechanics theory. This explanation is supported by introducing the effect of crack-tip stress shielding and the improved characterization of the stress field outside of a small-scale yield zone by means of Irwin's effective crack length, which yields results sim-

ilar to the values obtained by configurational forces. This has important consequences as neglecting the fracture process zone leads to predicting lower than actual toughness. For hydraulic fracturing applications, for example, this can hinder the process of parameters upscaling, which may result in underestimating toughness (Makhnenko et al., 2010). On the other hand, as shown in Table 2, the energy release rate computed from configurational forces tends to be closer to the one computed via the global approach as the structural size increases, and the entire problem tends toward linear elastic fracture mechanics.

Fig. 7 shows the damage distribution along with the vertical component of the configurational force vector field. The direction of the configurational forces is opposite to that of the crack propagation, and their magnitude is related to the energy release and dissipation rates, representing the energetic resistance to changing the material configuration (Maugin, 2016). Fracture propagation can be interpreted as a phase transition from intact to non-intact solid and the crack front as a moving boundary. The configurational forces highlight the phenomenon from an energetic point of view following classical Eshelby's approach. When damage reaches the maximum value at the notch tip, the crack boundary moves, as shown by the progressive evolution of damage.

6. Conclusions

From the previous analyses, we have provided evidence of the main failure mechanisms of Adelaide black granite. Micro-

structural features play a fundamental role in controlling the mechanisms of dissipation that lead to macroscopic failure. Through micro-imaging, we have shown the phenomenon of crack coalescence, which begins at the notch and in other stress concentration areas, such as grain boundaries, and tends to propagate along the cleavage planes in a zone of finite width.

By including this finite width as a non-local interaction, the numerical framework adopted has proved capable of representing the experimental results. Despite the fact that the three-point bending simulations were semi-blind predictions of the test data, we were able to simulate numerically the size dependency of the structural strength without over-parametrization and with a relatively simple non-local plastic-damage model. We have predefined the internal length of the non-local averaging scheme based on thin section photographs of the Adelaide black granite fractured area. This choice proved to be adequate: both the local behaviour, in terms of extension of the fracture process zone compared with acoustic emission data, and the global behaviour, in terms of the load-displacement curve, were correctly reproduced. Our conclusions are valid for the investigated geometry and for this set of self-similar structures; other testing configurations and other materials can provide additional support for the hypothesis underlying this study.

We have shown that numerical simulations are a valuable tool providing advanced interpretation of experimental results, shedding light on complex mechanisms and integrating the knowledge obtained from direct laboratory measurements. We have successfully applied non-local plastic-damage theory to explain the local evolution of the fracture process zone that was measured experimentally through acoustic emission. We have provided an advanced application of the theory of configurational mechanics, which has been employed to compute the energy release rate while taking into account the inelastic dissipation in the fracture process zone.

The limitations of the linear elastic fracture mechanics interpretation were clearly highlighted in both the experiments and the simulation. Whenever the fracture process zone is non-negligible compared with the specimen or structural size, global interpretation can become inaccurate, and only local non-linear analyses will lead to consistent and meaningful results.

Acknowledgements

Appendix A. Availability of the FEM code

The entire OpenGeoSys code employed for the analyses is freely available at

- https://github.com/ufz/ogs.git.

Several CTest are included with the distribution and their description is available at

- https://www.opengeosys.org/docs/benchmarks/.

These tests are performed to check the consistency of the numerical implementation whenever changes are made to the software and include a bar in traction, a beam in three-point bending conditions and a wide plate with holes under traction. The tests also serve the purpose of investigating the dependency of the solution on the mesh size, the time step size, the sensitivity to the linear solver convergence tolerance, the type of finite elements (triangles, quadrilaterals, tetrahedrons and hexahedrons), the order of element integration (linear, quadratic and cubic) and the order of the finite element approximation space (linear and quadratic). The described test results, which verify the numerical implementation under the aspects listed above, can be found in the code online documentation.

References

Barbier, E., 2002. Geothermal energy technology and current status: an overview. Renew. Sustain. Energy Rev. 6 (1), 3–65.

Barton, C.C., 1982. Variables in fracture energy and toughness testing of rock. in: The 23rd US symposium on rock mechanics (USRMS). Am. Rock Mech. Assoc..

Bažant P., Z., Jirásek, M., 2002. Nonlocal integral formulations of plasticity and damage: survey of progress. J. Eng. Mech. 128, 1119–1149.

Bažant, Z.P., 1984. Size effect in blunt fracture: concrete, rock, metal. J. Eng. Mech. 110 (4), 518–535.

Bažant, Z.P., Kazemi, M., 1990. Determination of fracture energy, process zone longth and brittleness number from size effect, with application to rock and conerete. Int. J. Fract. 44 (2), 111–131.

Bažant, Z.P., Planas, J., 1997. Fracture and Size Effect in Concrete and other Quasibrittle Materials. CRC press. 16.

Berto, F., Lazzarin, P., 2014. Recent developments in brittle and quasi-brittle failure assessment of engineering materials by means of local approaches. Mater. Sci. Eng.: R: Rep. 75, 1–48.

Bigoni, D., Dal Corso, F., Misseroni, D., Bosi, F., 2014. Torsional Locomotion. In: Proceedings of the Royal Society of London A: Mathematical, Physical and Engineering Sciences, Vol. 470, p. 20140599.

Biolzi, L., Labuz, J.F., Muciaccia, G., 2011. A problem of scaling in fracture of damaged rock. Int. J. Rock Mech. Min. Sci. 48 (3), 451–457.

Brooks, Z., Ulm, F.J., Einstein, H., 2012. Role of Microstructure Size in Fracture Process Zone Development of Marble. In: 46th US Rock Mechanics/Geomechanics Symposium. American Rock Mechanics Association.

Brooks, Z., Ulm, F.J., Einstein, H., 2013. Environmental scanning electron microscopy (ESEM) and nanoindentation investigation of the crack tip process zone in marble. Acta Geotech. 8 (3), 223–245.

Bunger, A., Kear, J, Rohde, A, Jeffrey, R, 2010. Hydraulic Fracture Growth Through Frictional Interfaces in Adelaide Black Granite: Phase I Experiments. CSIRO Report Number EP104290.

Cervera, M., Barbat, G., Chiumenti, M., 2017. Finite element modeling of quasi-brittle cracks in 2d and 3d with enhanced strain accuracy. Comput. Mech. 1–30.

Chambon, R., Caillerie, D., Matsuchima, T., 2001. Plastic continuum with microstructure, local second gradient theories for geomaterials: localization studies. Int. J. Solids Struct. 38, 8503–8527.

Chong, K., Li, V.C., Einstein, H., 1989. Size effects, process zone and tension softening behavior in fracture of geomaterials. Eng. Fract. Mech. 34 (3), 669–678.

Collin, F., Chambon, R., Charlier, R., 2006. A finite element method for poro mechanical modelling of geotechnical problems using local second gradient models. Int. J. Numer. Methods Eng. 65, 1749–1772.

Comi, C., 1999. Computational modelling of gradient-enhanced damage in quasi-brittle materials. Mech. Cohesive-Frictional Mater. 4, 17–36.

Council, N.R., 2013. Induced Seismicity Potential in Energy Technologies. National Academies Press.

Desmorat, R., Gatuingt, F., Jirásek, M., 2015. Nonlocal models with damage-dependent interactions motivated by internal time. Eng. Fract. Mech. 142, 255–275.

Dietsche, A., Steinmann, P., Willam, K., 1993. Micropolar elastoplasticity and its role in localization. Int. J. Plast. 9 (7), 813–831.

Duddu, R., Waisman, H., 2013. A nonlocal continuum damage mechanics approach to simulation of creep fracture in ice sheets. Comput. Mech. 1–14.

Eshelby, J.D., 1951. The force on an elastic singularity. Phil. Trans. R. Soc. Lond. A 244 (877), 87–112.

Evans, K., Moriya, H., Niitsuma, H., Jones, R., Phillips, W., Genter, A., Sausse, J., Jung, R., Baria, R., 2005. Microseismicity and permeability enhancement of hydrogeologic structures during massive fluid injections into granite at 3 km depth at the Soultz HDR site. Geophys. J. Int. 160 (1), 388–412.

Fakhimi, A., Tarokh, A., 2013. Process zone and size effect in fracture testing of rock. Int. J. Rock Mech. Min. Sci. 60, 95–102.

Fakhimi, A., Tarokh, A., Labuz, J.F., 2017. Cohesionless crack at peak load in a quasi-brittle material. Eng. Fract. Mech. 179, 272–277.

Fernandes, R., Chavant, C., Chambon, R., 2008. A simplified second gradient model for dilatant materials: theory and numerical implementation. Int. J. Solids Struct. 45, 5289–5307.

Geers, M., De Borst, R., Brekelmans, W., Peerlings, R., 1998. Strain-based transient–gradient damage model for failure analyses. Comput. Methods Appl. Mech. Eng. 160 (1–2), 133–153.

Giry, C., Dufour, F., Mazars, J., 2011. Stress-based nonlocal damage model. Int. J. Solids Struct. 48 (25), 3431–3443.

Grégoire, D., Verdon, L., Lefort, V., Grassl, P., Saliba, J., Regoin, J.P., Loukili, A., Pijaudier-Cabot, G., 2015. Mesoscale analysis of failure in quasi-brittle materials: comparison between lattice model and acoustic emission data. Int. J. Numer. Anal. Methods Geomech. 39, 1639–1664.

Grassl, P., Jirásek, M., 2006. Damage-plastic model for concrete failure. Int. J. Solids Struct. 43 (22), 7166–7196.

Grassl, P., Xenos, D., Jirásek, M., Horák, M., 2014. Evaluation of nonlocal approaches for modelling fracture near nonconvex boundaries. Int. J. Solids Struct. 51 (18), 3239–3251.

Gross, D., Kolling, S., Mueller, R., Schmidt, I., 2003. Configurational forces and their application in solid mechanics. Eur. J. Mech. A. Solids 22 (5), 669–692.

Guinea, G., Pastor, J., Planas, J., Elices, M., 1998. Stress intensity factor, compliance and cmod for a general three-point-bend beam. Int. J. Fract. 89 (2), 103–116.

Gurtin, M.E., 2008. Configurational Forces as Basic Concepts of Continuum physics, 137. Springer Science & Business Media.

Häring, M.O., Schanz, U., Ladner, F., Dyer, B.C., 2008. Characterisation of the basel 1 enhanced geothermal system. Geothermics 37 (5), 469–495.

Havlásek, P., Grassl, P., Jirásek, M., 2016. Analysis of size effect on strength of quasi-brittle materials using integral-type nonlocal models. Eng. Fract. Mech. 157, 172–185.

Horii, H., Nemat-Nasser, S., 1986. Brittle failure in compression: splitting, faulting and brittle-ductile transition. Philos. Trans. R. Soc.Lond. A: Math. Phys. Eng. Sci. 319 (1549), 337–374.

Houlsby, G.T., Puzrin, A.M., 2007. Principles of Hyperplasticity: An Approach to Plasticity Theory based on Thermodynamic Principles. Springer Science & Business Media.

Jankowski, L., Styś, D., 1990. Formation of the fracture process zone in concrete. Eng. Fract. Mech. 36 (2), 245–253.

Jirásek, M., 2004. Non-local damage mechanics with application to concrete. Failure Degrad. Instab. 683–707.

Jirásek, M., Marfia, S., 2005. Non-local damage model based on displacement averaging. Int. J. Numer. Methods Eng. 63, 77–102.

Kolditz, O., Bauer, S., Bilke, L., Böttcher, N., Delfs, J.O., Fischer, T., Görke, U.J., Kalbacher, T., Kosakowski, G., McDermott, C.I., Park, C.H., Radu, F., Rink, K., Shao, H., Shao, H.B., Sun, F., Sun, Y.Y., Singh, A.K., Taron, J., Walther, M., Wang, W., Watanabe, N., Wu, Y., Xie, M., Xu, W., Zehner, B., 2012. Opengeosys: an open-source initiative for numerical simulation of thermo-hydro-mechanical/chemical (THM/C) processes in porous media. Environ. Earth Sci. 67 (2), 589–599.

Kuhn, C., Lohkamp, R., Schneider, F., Aurich, J.C., Mueller, R., 2015. Finite element computation of discrete configurational forces in crystal plasticity. Int. J. Solids Struct. 56, 62–77.

Kuruppu, M., Obara, Y., Ayatollahi, M., Chong, K., Funatsu, T., 2014. ISRM-suggested method for determining the mode I static fracture toughness using semi-circular bend specimen. Rock Mech. Rock Eng. 47 (1), 267–274.

Labuz, J., Biolzi, L., 1998. Characteristic strength of quasi-brittle materials. Int. J. Solids Struct. 35 (31-32), 4191–4203.

Labuz, J., Shah, S., Dowding, C., 1985. Experimental analysis of crack propagation in granite. Int. J. Rock Mech. Mining Sci. & Geomechanics Abstracts 22 (2), 85–98.

Lakes, R.S., 2018. Stability of Cosserat solids: size effects, ellipticity and waves. J. Mech. Mater. Struct. 13 (1), 83–91.

Le, J.L., Bažant, Z.P., Bažant, M.Z., 2011. Unified nano-mechanics based probabilistic theory of quasibrittle and brittle structures: I. strength, static crack growth, lifetime and scaling. J. Mech. Phys. Solids 59 (7), 1291–1321.

Lemaitre, J., Chaboche, J. L., Benallal, A., Desmorat, R., 2009. Mécanique des matériaux solides-3eme édition. dunod.

Li, S., Wang, G., 2008. Introduction to Micromechanics and Nanomechanics. World Scientific Publishing Co Inc..

Liebe, T., Denzer, R., Steinmann, P., 2003. Application of the material force method to isotropic continuum damage. Comput. Mech. 30 (3), 171–184.

Lockner, D., Byerlee, J., Kuksenko, V., Ponomarev, A., Sidorin, A., 1991. Quasi-static fault growth and shear fracture energy in granite. Nature 350 (6313), 39–42.

Loret, B., Prevost, J.H., 1990. Dynamic strain localization in elasto-(visco-) plastic solids, part 1.general formulation and one-dimensional examples. Comput. Methods Appl. Mech. 83, 247–273.

Lyakhovsky, V., Hamiel, Y., Ben-Zion, Y., 2011. A non-local visco-elastic damage model and dynamic fracturing. J. Mech. Phys. Solids 59 (9), 1752–1776.

Maier, G., Hueckel, T., 1979. Nonassociated and coupled flow rules of elastoplasticity for rock-like materials. Int. J. Rock Mech. Mining Sci. & Geomech. Abstracts 16 (2), 77–92.

Makhnenko, R., Bunger, A., Detournay, E., 2010. Deviation from linear elastic fracture in near-surface hydraulic fracturing experiments with rock. in: 44th US rock mechanics symposium and 5th US-Canada rock mechanics symposium. Am. Rock Mech. Assoc..

Matsuki, K., Hasibuan, S., Takahashi, H., 1991. Specimen size requirements for determining the inherent fracture toughness of rocks according to the ISRM suggested methods. Int. J. Rock Mech. Mining Sci. & Geomech. Abstracts 28 (5), 365–374.

Maugin, G., 1998. On the structure of the theory of polar elasticity. philosophical transactions of the royal society of london a: mathematical. Phys. Eng. Sci. 356 (1741), 1367–1395.

Maugin, G.A., 1995. Material forces: concepts and applications. Appl. Mech. Rev. 48 (5), 213–245.

Maugin, G.A., 2016. Configurational Forces: Thermomechanics, Physics, Mathematics and Numerics. CRC Press.

McCarthy, G., White, W., Roy, R., Scheetz, B., Komarneni, S., Smith, D., Roy, D., 1978. Interactions between nuclear waste and surrounding rock. Nature 273 (5659), 216–217.

Metz, B., Davidson, O., De Coninck, H., Loos, M., Meyer, L., 2005. IPCC Special Report on Carbon Dioxide Capture and Storage. Tech. rep.. Working Group III.

Mihashi, H., Nomura, N., Niiseki, S., 1991. Influence of aggregate size on fracture process zone of concrete detected with three dimensional acoustic emission technique. Cem. Concr. Res. 21 (5), 737–744.

Mueller, R., Gross, D., Maugin, G., 2004. Use of material forces in adaptive finite element methods. Comput. Mech. 33 (6), 421–434.

Murakami, S., 2012. Continuum Damage Mechanics: AContinuum Mechanics Approach to the Analysis of Damage and Fracture. Springer Science & Business Media. 185.

Nagel, T., Görke, U.J., Moerman, K.M., Kolditz, O., 2016. On advantages of the kelvin mapping in finite element implementations of deformation processes. Environ. Earth Sci. 75 (11), 1–11.

Nagel, T., Kelly, D., 2012. Remodelling of collagen fibre transition stretch and angular distribution in soft biological tissues and cell-seeded hydrogels. Biomech. Model Mechanobiol. 11 (3–4), 325–339.

Nagel, T., Minkley, W., Böttcher, N., Naumov, D., Görke, U.J., Kolditz, O., 2017. Implicit numerical integration and consistent linearization of inelastic constitutive models of rock salt. Comput. Struct. 182, 87–103.

Needleman, A., 1988. Material rate dependence and mesh sensitivity in localization problems. Comput. Methods Appl. Mech. 67, 69–85.

Nguyen, G.D., 2011. A damage model with evolving nonlocal interactions. Int. J. Solids Struct. 48 (10), 1544–1559.

Nguyen, N.H., Bui, H.H., Nguyen, G.D., Kodikara, J., 2017. A cohesive damage-plasticity model for DEM and its application for numerical investigation of soft rock fracture properties. Int. J. Plasticity.

Niazi, M., Wisselink, H., Meinders, T., 2013. Viscoplastic regularization of local damage models: revisited. Comput. Mech. 51, 203–216.

Otsuka, K., Date, H., 2000. Fracture process zone in concrete tension specimen. Eng. Fract. Mech. 65 (2), 111–131.

Ouchterlony, F., 1990. Fracture toughness testing of rock with core based specimens. Eng. Fract. Mech. 35 (1), 351–366.

Özenç, K., Kaliske, M., Lin, G., Bhashyam, G., 2014. Evaluation of energy contributions in elasto-plastic fracture: a review of the configurational force approach. Eng. Fract. Mech. 115, 137–153.

Parisio, F., Laloui, L., 2017. Plastic-damage modeling of saturated quasi-brittle shales. Int. J. Rock Mech. Min. Sci. 93, 295–306.

Parisio, F., Naumov, D., Kolditz., O., Nagel, T., 2018. Material forces: an insight into continuum mechanics. Mech. Res. Comm. 93, 114–118.

Parisio, F., Samat, S., Laloui, L., 2015. Constitutive analysis of shale: a coupled damage plasticity approach. Int. J. Solids Struct. 75, 88–98.

Pijaudier-Cabot, G., Haidar, K., Dubé, J.F., 2004. Non-local damage model with evolving internal length. Int. J. Numer. Anal. Methods Geomech. 28 (7–8), 633–652.

Poh, L.H., Sun, G., 2016. Localizing gradient damage model with decreasing interactions. Int. J. Numer. Methods in Eng..

Rice, J.R., 1968. A path independent integral and the approximate analysis of strain concentration by notches and cracks. J. Appl. Mech. 35, 379–386.

Rutter, E., Neumann, D., 1995. Experimental deformation of partially molten westerly granite under fluid-absent conditions, with implications for the extraction of granitic magmas. J. Geophys. Res.: Solid Earth 100 (B8), 15697–15715.

Saroukhani, S., Vafadari, R., Simone, A., 2013. A simplified implementation of a gradient-enhanced damage model with transient length scale effects. Comput. Mech. 51 (6), 899–909.

Schmidt, R., Lutz, T., 1979. K^{Ic} and J^{Ic} of Westerly Granite–Effects of Thickness and In-plane Dimensions. In: Fracture mechanics applied to brittle materials. ASTM International.

Schmidt, R.A., 1976. Fracture-toughness testing of limestone. Exp. Mech. 16 (5), 161–167.

Simone, A., Wells, G.N., Sluys, L.J., 2003. From continuous to discontinuous failure in a gradient-enhanced continuum damage model. Comput. Methods Appl. Mech. Eng. 192 (41), 4581–4607.

Skarżyński, L., Tejchman, J., 2016. Experimental investigations of fracture process in concrete by means of x-ray micro-computed tomography. Strain 52 (1), 26–45.

Tarokh, A., Fakhimi, A., 2013. Relationship between Grain Size and Fracture Properties of Rock. 47th US Rock Mechanics/Geomechanics Symposium. American Rock Mechanics Association.

Tarokh, A., Fakhimi, A., 2014. Discrete element simulation of the effect of particle size on the size of fracture process zone in quasi-brittle materials. Comput. Geotech. 62, 51–60.

Tarokh, A., Fakhimi, A., Labuz, J., 2012. Size of Process Zone in Fracture Testing of Rock. 46th US Rock Mechanics/Geomechanics Symposium. American Rock Mechanics Association.

Tarokh, A., Makhnenko, R.Y., Fakhimi, A., Labuz, J.F., 2017. Scaling of the fracture process zone in rock. Int. J. Fract. 204 (2), 191–204.

Timmel, M., Kaliske, M., Kolling, S., 2009. Modelling of microstructural void evolution with configurational forces. ZAMM-J. Appl. Math. Mech./Zeitschrift für Angewandte Mathematik und Mechanik 89 (8), 698–708.

Vavro, L., Souček, K., Kytýř, D., Fíla, T., Keršner, Z., Vavro, M., 2017. Visualization of the evolution of the fracture process zone in sandstone by transmission computed radiography. Procedia Eng. 191, 689–696.

Violay, M., Heap, M., Acosta, M., Madonna, C., 2017. Porosity evolution at the brittle–ductile transition in the continental crust: implications for deep hydro-geothermal circulation. Sci. Rep. 7 (1), 7705.

Wang, C., Peide, L., Rongsheng, H., Xiutang, S., 1990. Study of the fracture process zone in rock by laser speckle interferometry. Int. J. Rock Mech. Mining Sci. & Geomech. Abstracts 27 (1), 65–69.

Watanabe, N., Egawa, M., Sakaguchi, K., Ishibashi, T., Tsuchiya, N., 2017. Hydraulic fracturing and permeability enhancement in granite from subcritical/brittle to supercritical/ductile conditions. Geophys. Res. Lett..

Watanabe, N., Numakura, T., Sakaguchi, K., Saishu, H., Okamoto, A., Ingebritsen, S.E., Tsuchiya, N., 2017. Potentially exploitable supercritical geothermal resources in the ductile crust. Nat. Geosci. 10 (2), 140–144.

Wegst, U.G., Bai, H., Saiz, E., Tomsia, A.P., Ritchie, R.O., 2015. Bioinspired structural materials. Nat. Mater. 14 (1), 23–36.

Wu, Z., Rong, H., Zheng, J., Xu, F., Dong, W., 2011. An experimental investigation on the FPZ properties in concrete using digital image correlation technique. Eng. Fract. Mech. 78 (17), 2978–2990.

Xenos, D., Grégoire, D., Morel, S., Grassl, P., 2015. Calibration of nonlocal models for tensile fracture in quasi-brittle heterogeneous materials. J. Mech. Phys. Solids 82, 48–60.

Zang, A., Wagner, F.C., Stanchits, S., Janssen, C., Dresen, G., 2000. Fracture process zone in granite. J. Geophys. Res.: Solid Earth 105 (B10), 23651–23661.

Zietlow, W.K., Labuz, J., 1998. Measurement of the intrinsic process zone in rock using acoustic emission. Int. J. Rock Mech. Min. Sci. 35 (3), 291–299.